Multiobjective Design Exploration of Propeller Airfoils at Low-Reynolds and High-Mach Number Conditions towards Mars Airplane

By Seiichiro Morizawa,[1] Taku Nonomura,[2] Shigeru Obayashi,[1] Akira Oyama[2] and Kozo Fujii[2]

[1] *Tohoku University, Sendai, Japan*
[2] *Institute of Space and Astronautical Science, JAXA, Sagamihara, Japan*

Multiobjective design explorations of airfoils for Mars airplane propeller blade are conducted to obtain insights into high efficiency Mars airplane propeller blade design in low Reynolds number and high Mach number condition. In this study, two airfoil design optimization problems at different Mach number in low Reynolds number condition are studied to understand the Mach number effect. Maximization of the lift coefficient and minimization of the drag coefficient are employed as the objective functions where the design valuables are control points of B-spline curves representing airfoil shape. The result of multiobjective aerodynamic optimization suggests that non-dominated solutions in low and high Mach number conditions have a similar trend, although these solutions in low Mach number condition are widely scattered. Dominant modes of non-dominated solutions relates with the large aft camber and thick near middle region of airfoil geometry when the Mach number is larger. The larger aft camber is observed as the common feature of the non-dominated solutions, and three-representative airfoils for minimum C_d, maximum l/d, and maximum C_l designs among the non-dominated solutions have a similar shape. The geometry becomes thicker the near middle region of the airfoil due to the Mach number effect.

Key Words: Mars Airplane, Airfoil, Propeller, Multiobjective Design Exploration, Computational Fluid Dynamics

Nomenclature

α	:	angle of attack
C	:	chord length of airfoil
Re	:	Reynolds number
M	:	Mach number
C_f	:	local skin-friction coefficient
C_p	:	surface pressure coefficient
C_l	:	lift coefficient
C_d	:	drag coefficient
l/d	:	lift-to-drag
R	:	propeller radius
x	:	coordinate in chordwise direction
z	:	coordinate in normal direction

1. Introduction

The use of an airplane is an attractive approach for the Martian surface observation and atmosphere analysis because an airplane can provide higher resolution data than an orbital satellite and larger spatial coverage than a ground-based rover. Feasibility study of the Mars airplane for Mars exploration by the air vehicle working group in Japan Aerospace Exploration Agency (JAXA) suggests that further technology developments are required to realize the Mars airplane.[1] High efficiency propeller-based propulsion system is one of them.

Propellers of the Mars airplane are operated in the special condition. First, the operating Reynolds number condition is lower than that of the Earth because (1) the air density on the Mars is approximately one-hundredth lower than that on the Earth, and (2) the size of the Mars airplane is restricted to be small because the airplane must be stored into an aeroshell delivered by a launcher. The order of the Reynolds number based on the chord length of Mars airplane propeller blade corresponds 10^3 to 10^4. In such low Reynolds number conditions, it is known that the aerodynamic performance of an airfoil is significantly inferior to that in higher Reynolds number conditions because the viscous effect is dominant. As the Reynolds number decreases, a rapid decrease in the lift-to-drag ratio and the lift coefficient, and an increase in the drag coefficient are observed.[2] In Ref-3), a remarkable difference of lift-to-drag ratio between NACA4402 and NACA4404 airfoils was reported in the low Reynolds number condition. Kunz and Kroo numerically investigated the effects on several airfoil geometry parameters in the low Reynolds number conditions for various members of the NACA four-digit airfoil family.[4] These results indicate that the geometry variations still have significant effects on the aerodynamic performance in such low Reynolds number conditions.

At the same time, propellers of the Mars airplane are also operated in high Mach number conditions because the speed of sound on the Mars is lower that on the Earth due to lower temperature and difference in atmospheric composition (the carbon dioxide occupies more than 95% of atmospheric gas in the Mars). To develop a high efficiency propulsion system with sufficient thrust, it is necessary to design a propeller considering Mach number effects in the low Reynolds number condition. However, there are few studies on aerodynamic airfoil design in such conditions.

The aim of this study is to understand Mach number effect on the propeller profile shape design in low Reynolds number. In this study, multiobjective profile shape design optimization

problems at different Mach number are studied with multiobjective design exploration based on evolutionary computation and computational fluid dynamics.

2. Approach

2.1. Design optimization problem

The propeller blade designed by Hayashida and Sunada[5] for a Mars airplane is considered here (Fig. 1). This propeller adopts a thin triangular airfoil.[6] The local Mach and Reynolds numbers at each section are summarized in Table 1. The design angle of attack is 6.5° from the root to the tip because maximum lift-to-drag ratio of the triangular airfoil is obtained at this angle of attack.[6]

In this study, multiobjective aerodynamic optimizations of the propeller profile shape at different Mach number are conducted to understand Mach number effects on the profile shape design in low Reynolds number condition. The design conditions are shown in Table 2, each of which corresponds to the operating conditions at root ($r/R = 0$) and near tip ($r/R = 0.975$), respectively.
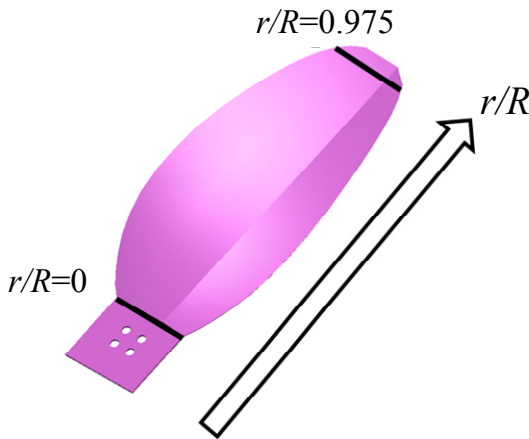

Fig. 1.   Definition of radial position of propeller blade.

Table 1.   Local M and local Re at each section.

r/R	Re	M_∞	α
0	**2318**	**0.254**	**6.5°**
0.063	3206	0.268	6.5°
0.375	5990	0.365	6.5°
0.688	6680	0.485	6.5°
0.875	5648	0.562	6.5°
0.975	**3298**	**0.604**	**6.5°**
1.000	0	0.615	6.5°

Table 2.   Design conditions.

Case	Re	M	α
Case 1 ($r/R = 0$)	3000	0.6	6.5°
Case 2 ($r/R = 0.975$)	3000	0.2	6.5°

Design objectives are maximization of the lift coefficient and minimization of the drag coefficient. It is very important to understand tradeoff between maximization of the lift coefficient and minimization of the drag coefficient because

lift coefficient mainly contributes to thrust coefficient and the drag coefficient mainly contributes to torque coefficient, where smaller torque coefficient means lighter motor weight (motor is one of the heaviest equipment of the Mars airplane system). Here, the constraint condition $C_l < 1$ is applied because very high lift coefficient airfoil design has an unacceptably large drag coefficient.

The airfoil shape is parameterized with B-spline curves (Fig. 2). These curves are determined by nine control points where the control points at the leading and trailing edges are fixed. Here, x and z coordinates of the other six control points are considered at the design parameters. A total number of the design variables are twelve. Table 3 shows the search region of each design variable.
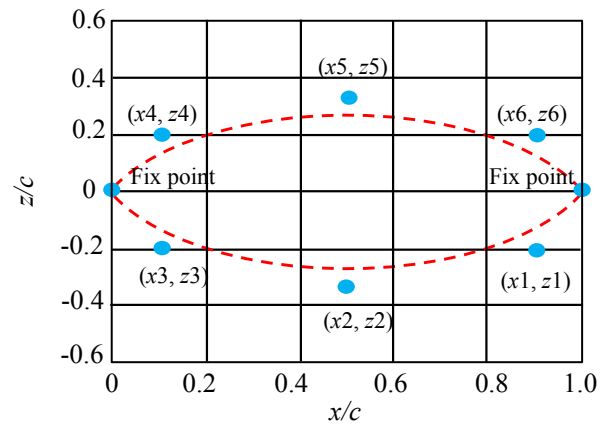

Fig. 2.   Airfoil shape parameterization.

Table 3.   Search region of each design valuable.

Design variables	Lower band	Upper band
$x1$	0.66	0.99
$x2$	0.33	0.66
$x3$	0.001	0.33
$x4$	0.001	0.33
$x5$	0.33	0.66
$x6$	0.66	0.99
$z1$	-0.1	0.2
$z2$	-0.1	0.2
$z3$	-0.1	0.2
$z4$	-0.05	0.4
$z5$	-0.05	0.4
$z6$	-0.05	0.4

2.2. Aerodynamic force evaluation

The governing equations are the two-dimensional compressible Navier-Stokes equations, which is normalized by the chord length of the airfoil, the density and the sound speed of the freestream, respectively. These equations are solved in the curvilinear coordinate system. Numerical fluxes for convective terms are evaluated by the simple higher-resolution upwind scheme,[7] extended to third-order space accuracy by the monotone upwind scheme for conservation low interpolation.[8] The viscous terms are computed by a second central difference scheme. The second-order backward differencing is converged by the three

iterations of alternative-directional-implicit symmetric-Gause-Seidel scheme[9] for time integration. The flow fields are considered to be laminar in the entire region.

For each design, C-typed grid is generated using algebraic method. As a result of grid convergence studies of several airfoils with three different grids: 249×51, 497×101, and 615×101, 249 (chordwise direction) ×51 (normal direction) grid is adopted.

2.3. Multiobjective aerodynamic optimization

Non-dominated sorting genetic algorithm-II (NSGA-II)[10] is used for multiobjective aerodynamic optimization. Here, NSGA-II is a fast and elitist multiobjective evolutionary algorithm proposed by Deb *et al*. Flowchart of the current optimization is shown in Fig. 3. The initial population is created randomly, and this population is evaluated by computational fluid dynamics (CFD) simulations and sorted based on Goldberg's Pareto-ranking.[11] Binary tournament selection in reproductive selection is used to select the pairs of parents, and blended crossover[12] and polynomial mutation[13] are used to create a child population. Then, the child population is evaluated with CFD simulations and the best half is selected from the combined population of the parent population and the child population based on the non-dominated sorting. Crossover rate, crossover index, mutation ratio, and mutation index are set to 1.0, 15, 0.1, and 25, respectively. The size of population and the number of generation are set to 100 and 42, respectively.
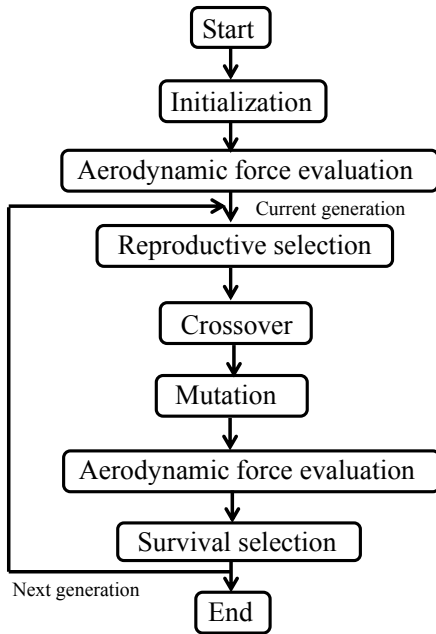

Fig. 3. Flowchart of optimization.

2.4. Data mining

In this study, proper orthogonal decomposition (POD) is used to the airfoil shape of the non-dominated solutions as in Ref-14). As described in Ref-15), POD enables direct analysis of airfoil shape of Pareto-optimal designs. When the design parameters of airfoils are analyzed, it is often difficult to understand effect of shape difference on the flow due to interaction among the design parameters.

In POD, the data to be analyzed are decomposed into the mean vector and the fluctuation vector because analysis of the fluctuation from the mean vector maximizes variance of the data. In this study, the x and z coordinates of all the grid points on the airfoil shape are used. Here, the shape data of non-dominated solutions are decomposed into the averaged data and fluctuation as follows.

$$\begin{bmatrix} r(1,n) \\ r(2,n) \\ \vdots \\ r(j\max-1,n) \\ r(j\max,n) \end{bmatrix} = \begin{bmatrix} r_{ave}(1) \\ r_{ave}(2) \\ \vdots \\ r_{ave}(j\max-1) \\ r_{ave}(j\max) \end{bmatrix} + \begin{bmatrix} r'(1,n) \\ r'(2,n) \\ \vdots \\ r'(j\max-1,n) \\ r'(j\max,n) \end{bmatrix} \quad (1)$$

The fluctuation vector is then expressed by the linear sum of the normalized eigenvectors and orthogonal base vectors as follows:

$$\begin{bmatrix} r'(1,n) \\ r'(2,n) \\ \vdots \\ r'(j\max-1,n) \\ r'(j\max,n) \end{bmatrix} = a_1(n)\begin{bmatrix} r'_{base}(1,1) \\ r'_{base}(2,1) \\ \vdots \\ r'_{base}(j\max-1,1) \\ r'_{base}(j\max,1) \end{bmatrix} + \cdots + a_{m\max}(n)\begin{bmatrix} r'_{base}(1,m\max) \\ r'_{base}(2,m\max) \\ \vdots \\ r'_{base}(j\max-1,m\max) \\ r'_{base}(j\max,m\max) \end{bmatrix} \quad (2)$$

where each eigenvector is determined such that the energy defined by Eq. (3) is maximized.

$$\sum_{j=1}^{j\max} r'^2_{base}(j,m), \qquad m = 1, 2, ..., \max \quad (3)$$

The eigenvector that maximizes the energy defined by Eq. (3) can be obtained by solving the eigenvalue problem of the following covariance matrix:

$$\begin{pmatrix} S_{1,1} & \cdots & S_{m1,1} & \cdots & S_{m\max,1} \\ \vdots & \ddots & & & \vdots \\ S_{1,m2} & \cdots & S_{m1,m2} & & S_{m\max,m2} \\ \vdots & & & \ddots & \vdots \\ S_{1,m\max} & \cdots & S_{m1,m\max} & \cdots & S_{m\max,m\max} \end{pmatrix} \quad (4)$$

where

$$S_{m1,m2} = \sum_{j=1}^{j\max} r'(j,m1)r'(j,m2) \quad (5)$$

Then, the i-th eigenvector in Eq. (4) is corresponding to the orthogonal base function vector (i-th POD mode vector; i is POD mode number).

3.   Results

3.1.   Comparison of non-dominated solutions

Non-dominated solutions of case 1 (low *Re* and high *M* condition) and case 2 (low *Re* and low *M* condition) are compared in Fig. 4 to see the difference in the Pareto-fronts. There is no significant difference between the two distributions though the non-dominated solutions of case 1 are narrowly scattered. This implies the Mach number effects in low *Re* conditions on the non-dominated solutions between lift and drag coefficients are small.

Next, the airfoil shapes of non-dominated solutions of cases 1 and case 2 are analyzed with POD. Figure 5 shows the energy ratios of principal orthogonal base vectors (i.e. principle POD modes) to the total energy. In both cases, the similar distributions of these modes are observed, and the first and second modes are dominant. Therefore, we can assume that analysis of modes 1 and 2 is enough (about 95% in both cases).

Figure 6 shows the components of the eigenvectors of the non-dominated airfoil designs of cases 1 and 2, where $a_1(n)$ and $a_2(n)$ correspond to the expansion coefficients in Eq. (2). The horizontal axis corresponds to that of Fig. 4. From this figure, we observe that there are three groups in the non-dominated airfoil designs of both cases: low drag designs, high *l/d* designs, and high lift designs. As for case 1, the eigenvectors of both modes of the low drag design group are positive in general. Among the high *l/d* design group, the eigenvector of the first mode is negative and gradually increases as the lift coefficient increases while the eigenvector of the second mode is roughly zero. As for the high lift design group, the eigenvector of the first mode is positive and the eigenvector of the second mode is negative. In case 2, low drag designs have positive second component of the eigen vectors while high *l/d* design have negative second component. The first component gradually decreases among these groups. The high lift designs have negative first mode and positive second mode.

Figure 7 shows the averaged airfoil shape of non-dominated solutions and the orthogonal base vectors of the first and second modes (vectors in the right hand side of Eq. (2)). This figure shows that the first mode of case 1 mainly contributes to the camber change near the trailing edge while the second mode of case 1 contributes to the camber change from the leading to the trailing edges. As for case 2, the first mode contributes to the camber line and thickness distribution and the shape difference is larger than that in case 1.

Recalling that the shapes of the non-dominated solutions are represented by Eqs. (1) and (2), Figs 6 and 7 indicate that high *l/d* designs in case 1 has thinner thickness in the front part and smaller maximum chamber the trailing edge. As for the case 2, low drag designs have lower maximum camber while high lift designs have higher maximum camber and larger thickness in the front part.

The airfoil shapes of the minimum C_d, maximum *l/d*, and maximum C_l designs are shown in Fig. 8. The minimum C_d airfoil has common features such as relatively small camber, thin leading edge and thick trailing edge. The maximum *l/d*

airfoil also has common features such as relatively large camber, maximum camber near the trailing edge, thin leading edge and thick trailing edge. The maximum C_l airfoil has also large camber with maximum camber near the trailing edge but the thickness distributions are different. The maximum C_l airfoil in case 1 has a thick leading edge while that in case 2 has a thin leading edge.
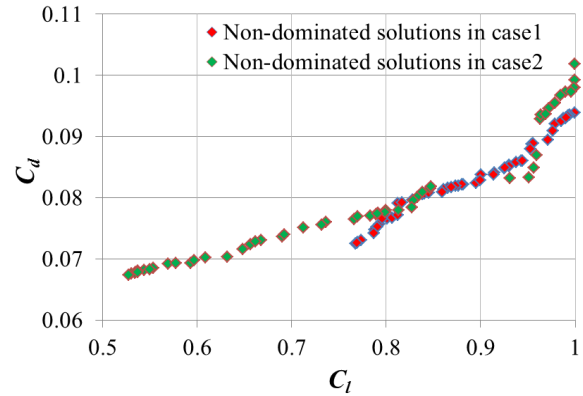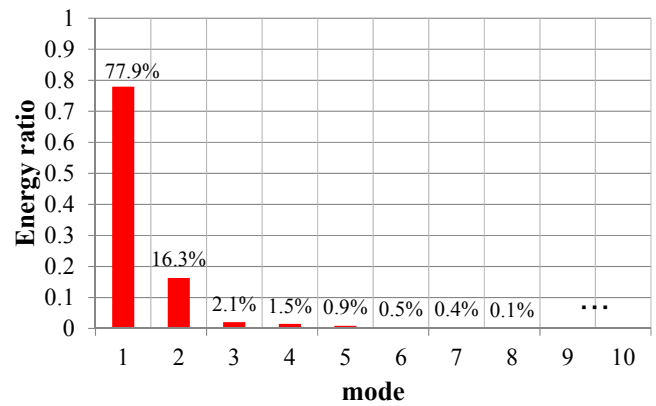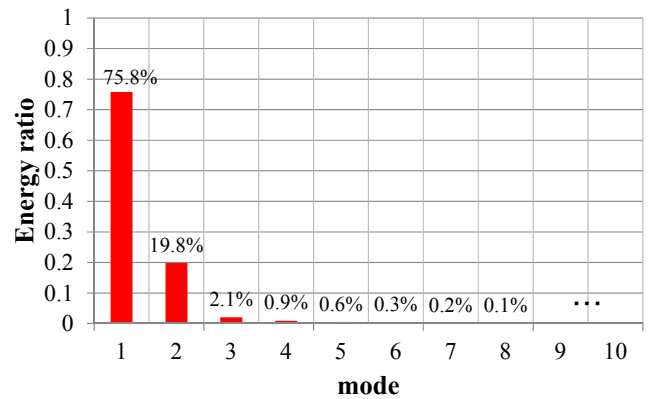

Fig. 4.   Comparison of non-dominated solutions between case 1 (low *Re* and high *M* condition) and case 2 (low *Re* and low *M* condition).
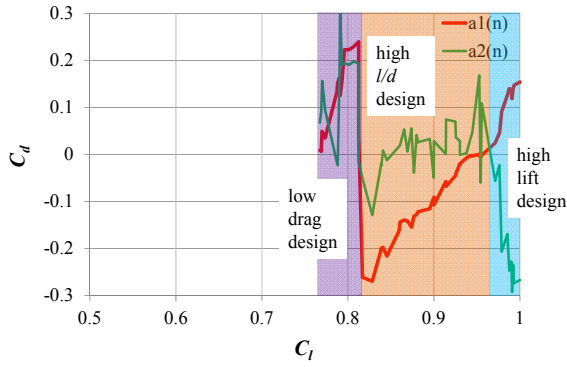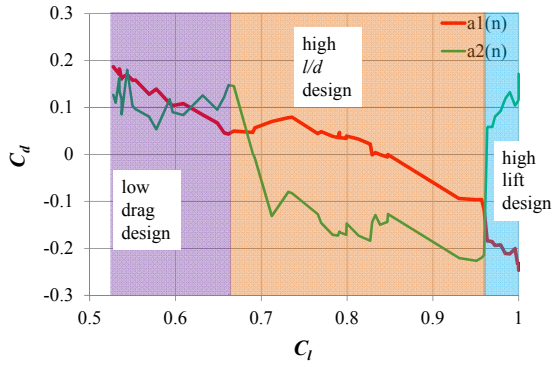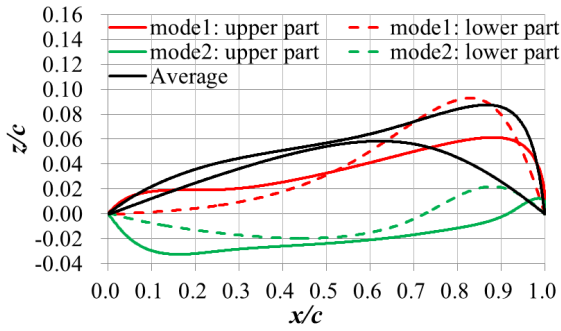

(a) Case 1

(b) Case 2

Fig. 5.   Comparison energy ratio between case 1 (low *Re* and high *M* condition) and case 2 (low *Re* and low *M* condition).
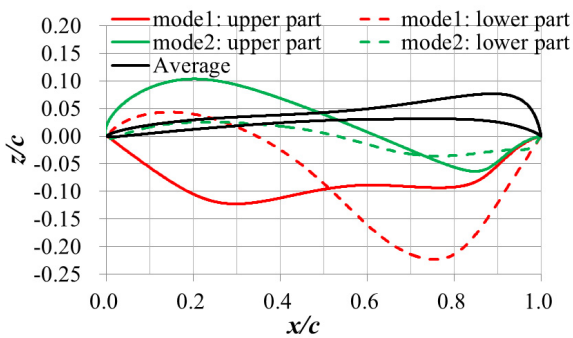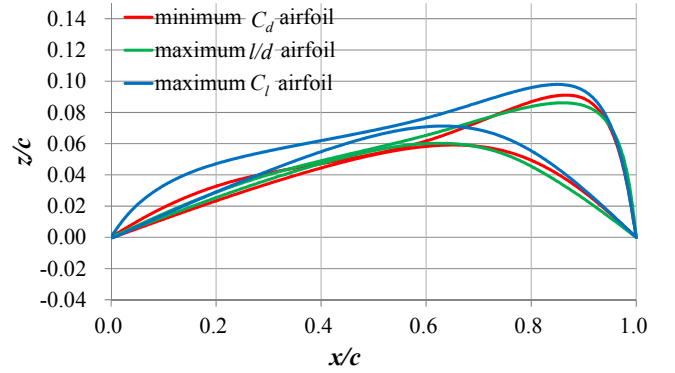
(a) Case 1

(b) Case 2

Fig. 6.   Comparison of the eigenvector with respect n between case 1 (low Re and high M condition) and case 2 (low Re and low M condition).
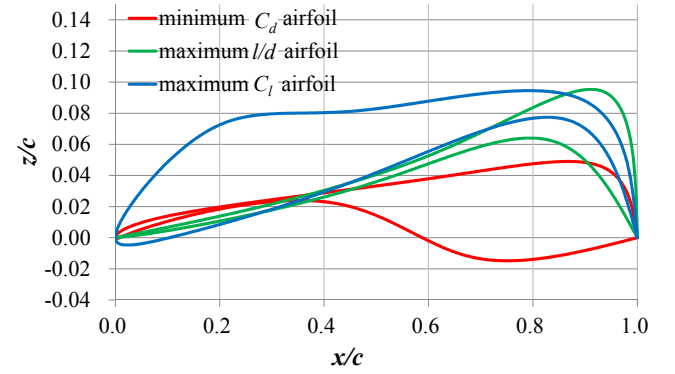

(a) Case 1

(b) Case 2

Fig. 7.   Comparison orthogonal base vector between case 1 (low Re and high M condition) and case 2 (low Re and low M condition).

(a) Case 1

(b) Case 2

Fig. 8.   Comparison of airfoil shapes between case 1 (low Re and high M condition) and case 2 (low Re and low M condition).

3.2.   Flow analysis of the representative non-dominated airfoils

The C_p and C_f distributions of the minimum C_d, maximum l/d, and maximum C_l airfoils in cases 1 and 2 are shown in Figs. 9 and 10, respectively. The C_p distributions of these airfoils in case 1 are almost similar except for the suction region of the leading edge, while those in case 2 are completely different. The airfoils of maximum l/d, and maximum C_l designs in case 2 have relatively the flat C_p distributions on upper surface after the suction region, and this distribution of the maximum C_l airfoil is especially prominent. In addition, the C_f distributions of these airfoils in case 1 are also similar, and the difference of those in case 2 becomes larger. The maximum l/d airfoil in case 2 has a rapid decrease of the C_f distribution where the end of the flat C_p distribution mentioned above occurs near the trailing region.

Figures 11 and 12 show the instantaneous vorticity of cases 1 and 2 of three-representative airfoils in non-dominated solutions mentioned above. The flow fluctuation around airfoil is comparatively small in all airfoils though the wake region on flow field of minimum C_d airfoil is different. On the other hand, as shown in Fig. 12, the vortex shedding of upper surface at the leading edge occurs in all airfoils. Among them, the unsteady fluctuations of airfoils, such as airfoils with maximum C_l or l/d, are also observed on the lower surface.

Then, the reattachment of this flow separation on upper surface is observed at the trailing edge of the maximum l/d airfoil.

These results suggest that the variation of these airfoils become smaller by Mach number effects in low Re condition, and the flow fields of these airfoils are stabilized when the Mach number is higher. Then, the difference in C_p and C_f distribution on the airfoil surfaces becomes smaller. Therefore, the Mach number effect leads to robust aerodynamic performance among their representative airfoils mentioned above because geometry variation is small.
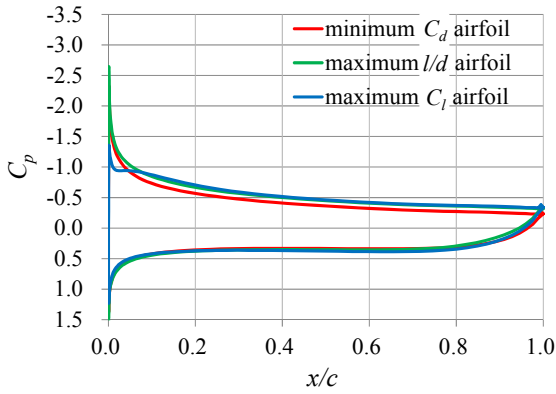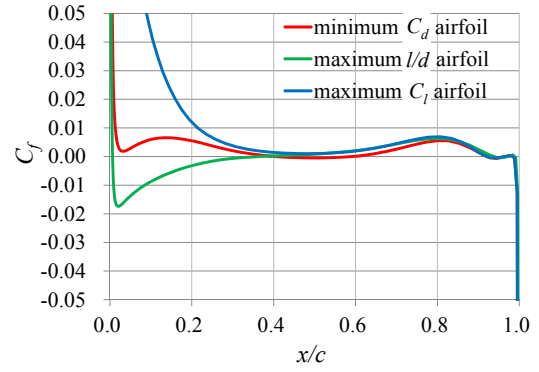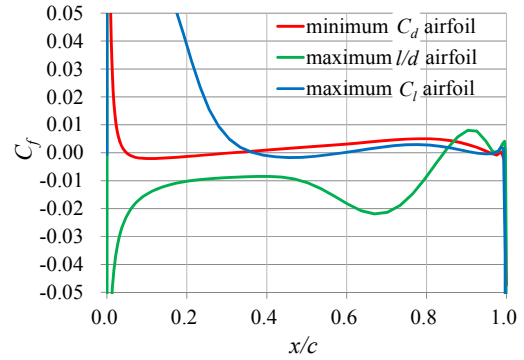

(a) Case 1
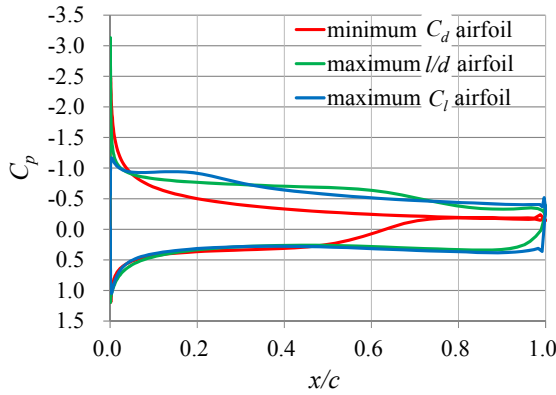
(b) Case2

Fig. 9. Comparison C_p distribution between case 1 (low Re and high M condition) and case 2 (low Re and low M condition).
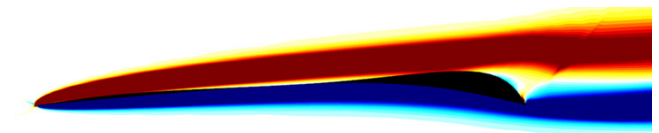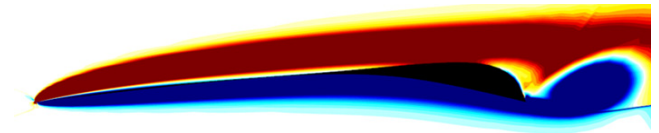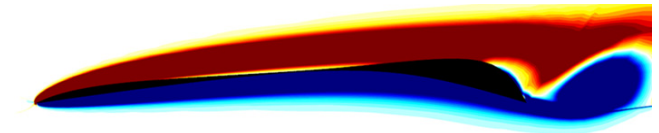

(a) Case 1

(b) Case 2

Fig. 10. Comparison C_f distribution between case 1 (low Re and high M conditions) and case 2 (low Re and low M conditions).

(a) Minimum C_d airfoil

(b) Maximum l/d airfoil

(c) Maximum C_l airfoil

$$-5 \leq \omega_y \leq 5$$

Fig. 11. Snapshots of instantaneous vorticity distributions of non-dominated solutions in case 1 (low Re and high M condition).

(a) Minimum C_d airfoil

(b) Maximum l/d airfoil

(c) Maximum C_l airfoil
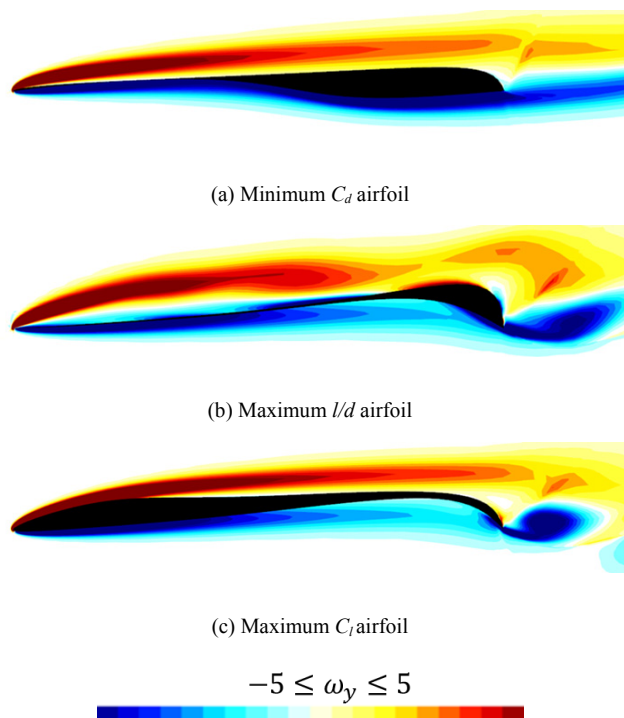
$$-5 \leq \omega_y \leq 5$$

Fig. 12.   Snapshots of instantaneous vorticity distributions of non-dominated solutions in case 2 (low Re and low M condition).

4.   Conclusions

Multiobjective design exploration of airfoils is conducted to obtain useful information of aerodynamic design for Mars airplane propeller blade. For this purpose, the comparison of aerodynamic optimization between the low Re and high M condition (near tip condition) and low Re and low M condition (near root condition) is conducted to investigate the Mach number effects at the low Reynolds number conditions. Next, proper orthogonal decomposition (POD) is applied to the airfoil shapes of the non-dominated solutions under these conditions, and the information of airfoil shapes on the non-dominated solutions are extracted. Then, the comparisons of Mach number effects on the three-representative airfoils, such as the minimum C_d, maximum l/d, and maximum C_l designs, are also conducted.

The result of aerodynamic optimization suggests that Mach number effects in low Re conditions on the distributions of non-dominated solutions are small though the non-dominated solutions of the low Re and high M condition are narrowly scattered. Next, the result of POD suggests that dominant modes of non-dominated solutions relate with the large aft camber and thick near middle region of airfoil geometry when the Mach number is larger. Then, the common feature of the three-representative airfoils on non-dominated solutions is observed in the geometry of larger aft camber except for minimum C_d design in the near root condition. On the other hand, the representative airfoil shapes in the tip condition have almost similar shapes because flow fields are stabilized by Mach number effect. Therefore, robust aerodynamic performance among these representative airfoils is observed in the low-Reynolds number condition considering Mach number effects.

References

1) Oyama, A., Nagai, H., Takeuchi, S., Toyoda, H., Sunada, S., Tokutake, H., Ogawa,H., Toda, K., Koike, M., Motoda, T., Fujita, K. and Mars Exploration Aircraft WG.: Small Size Airplane Exploration, Proceedings of the 42th JSASS Annual Meeting, Apr. 2012 (in Japanese).
2) McMasters, J. H. and Henderson, M. L.: Low Speed Single Element Airfoil Synthesis, *Technical Soaring*, **6** (1980), pp. 1-21.
3) Kunz, J. P. and Strawn, C. R.: Analysis and Design of Rotors at Ultra-Low Reynolds Numbers, AIAA paper 2002-0099, 2002.
4) Kunz, P. J. and Kroo, I.: Analysis and Design of Airfoils for Use at Ultra-Low Reynolds Numbers, *Fixed and Flapping Wing Aerodynamics for Micro Air Vehicle Applications, Mueller, T. J.,(ed.),* Vol. 195, Progress in Aeronautics and Astronautics, AIAA, Reston, VA, 2001, pp. 35-60.
5) Hayashida, T. and Sunada, S.: Design of a Propeller on Mars, 49th Aircraft symposium, Oct. 2011 (in Japanese).
6) Suwa, T., Nose, K., Numata, D., Nagai, H. and Asai, K.: Compressibility Effects on Airfoil Aerodynamics at Low Reynolds Number, AIAA paper 2013-3029, 2013.
7) Shima, E., and Jounouchi, T.: Role of CFD in Aeronautical Engineering (No.14)-AUSM Type Upwind Schemes, Proceeding of the 14th NAL Symposium on Aircraft Computational Aerodynamics, June 1997.
8) Van L., B.: Towards the Ultimate Conservative Difference Scheme, IV. A New Approach to Numerical Convection, *Journal of Computational Physics*, **23** (1977), pp. 276-299.
9) Fujii, K.: Simple Ideas for the Accuracy and Efficiency Improvement of the Compressible Flow Simulation Methods, Proceedings of the International CFD Workshop on Supersonic Transport Design, Mar. 1998.
10) Deb, K., Pratap, A., Agarwal, S. and Meyarivan, T.: A fast and elitist multiobjective genetic algorithm: NSGA-II, Evolutionary Computation, *IEEE Transactions,* **6** (2002), pp.182-197.
11) Goldberg, D.E.: *Genetic Algorithms in Search, Optimization and machine Learning*, Addison Wesley, 1989.
12) Eshelman, L. J. and Schaffer, J. D.: Real-Coded Genetic Algorithms and Interval Schemata, Foundations of Genetic Algorithms 2, Morgan Kaufmann, San Mateo, CA, (1993), pp. 187–202.
13) Deb, K. and Goyal, M.: A Combined Genetic Adaptive Search (geneAS) for Engineering Design, *Computer Science and Informatics*, **26 (4),** (1996), pp.30-45.
14) Sirovich, L.: Turbulence and Dynamics of Coherent Structures Part 1: Coherent Structures, *Quarterly of Applied Mathematics*, **45** (1987), pp.561-571.
15) Oyama, A., Nonomura, T. and Fujii, K.: Data Mining of Pareto-Optimal Transonic Airfoil Shapes Using Proper Orthogonal Decomposition," *Journal of Aircraft*, **47** (2010), pp.1756-1762.